Kerr Microcombs in Integrated Waveguide Ring Resonators Enabled by Graphene Nonlinearity

Alexandros Pitilakis, *Senior Member, IEEE*, and Emmanouil E. Kriezis, *Senior Member, IEEE*

***Abstract*—We theoretically demonstrate the generation of Kerr microcombs in integrated graphene-clad silicon-nitride slot waveguide ring resonators. In our work, the graphene monolayer provides the enabling nonlinearity, by means of its third-order surface conductivity. We use the Lugiato-Lefever equation framework, modified to incorporate the frequency dispersion of all eigenmode properties—including nonlinearity—in an ultrawide octave-spanning spectrum. The waveguide parameters are rigorously computed by a full-vector mode solver where we input graphene's full set of electromagnetic properties, both linear and nonlinear; the latter are extracted by quantum perturbation formulas, as a function of graphene's chemical potential and equilibrium lattice temperature. Our results show the potential of graphene, as a 2D material with electrically tunable linear and nonlinear response, for Kerr combs or other integrated nonlinear devices, such as mode-locked and Q-switched lasers.**

***Index Terms*—Kerr microcomb, graphene, ring resonator, integrated waveguide, silicon nitride, electro-optic, nonlinear optics.**

I. INTRODUCTION

KERR optical frequency combs (OFC) [1], [2], [3] can be generated by coupling a CW pump laser into a dispersive and nonlinear travelling-wave resonator, Fig. 1. Under specific conditions, the counter-action between group velocity dispersion (GVD) and Kerr-type refractive nonlinearity gives rise to pulse-train output from the resonator, whose spectrum is an OFC, i.e., a set of equidistant 'teeth' separated by the free-spectral range (FSR) of the cavity. An OFC is also defined by the balance between the cavity's aggregate attenuation, which is inversely proportional to its quality (Q) factor, and the parametric gain imparted by external pumping and cascaded four-wave mixing (FWM). Evidently, high values in nonlinearity, Q-factor, and optical confinement are the desired features for the resonator. The most frequently used resonators for Kerr OFC are bulk whispering-galleries, e.g., magnesium fluoride micropillars [4], [5], designed for very high Q-factors and critically coupled to optical fibers. As contemporary practical applications shift towards photonic integrated circuits (PIC), waveguide ring resonator (WRR) Kerr combs have also appeared [6], [7], underpinned by the same principles but also requiring for redesign to exploit the stronger light-matter interaction in integrated nanophotonics. In all resonator platforms, bulk or PIC, the external-control circuitry typically involves one or multiple pump lasers, whose frequency and amplitude can be accurately controlled in a timescale comparable to the roundtrip time, $t_R = 1/\mathrm{FSR}$. The performance of an OFC can be quantified by its footprint, FSR, spectral span (number of teeth), and pumping threshold power. Applications of OFCs include interconnects [8], massively parallel coherent communications [9], RF photonics [10], ultrafast distance and velocity measurements using light (LiDAR) [11], [12], chip-scale atomic clocks [13], dual-microcomb spectroscopy [14], low noise microwave generation [15], integrated optical frequency synthesizers [16], and extremely precise astrophysical measurements [17].

Graphene is an emerging 2D semiconductor material with high expectations for diverse applications at optical frequencies [18], compatible with standard silicon-photonic technology, allowing for electro-optical control (EOC) over its response in an ultrawide spectral window [19], [20], [21], and exhibiting a high third-order nonlinearity [22], [23], [24], [25]. These features paved the road towards recent advances in nonlinear applications of graphene-comprising integrated photonic waveguide devices [26], [27], demonstrating its high potential for Kerr OFCs. From a PIC technology perspective, enhanced light-graphene interaction and dispersion engineering, both cornerstones of Kerr OFCs, are essentially waveguide engineering tasks. Additionally, in graphene-comprising (GC) waveguides, we gain access to extra degrees of freedom, namely the high nonlinearity from the 2D material and the EOC over both its linear and nonlinear properties, albeit in a coupled manner. The recent literature touching upon the generation of Kerr OFCs in such electro-optically controlled PICs consisting of graphene overlaid WRRs is relatively limited: B. Yao et al. presented so-far the only experimentally measured Kerr comb in a PIC-GC-WRR [28], where EOC is used to tune the dispersion of the cavity and thus the output OFC; theoretical and numerical works [29], [30], [31] present designs and analyses of EOC-PIC-GC-WRR. We note, however, that none of the above works rigorously considers graphene's *own* nonlinearity, much less its spectral dispersion.

In this work we show that graphene's nonlinear surface conductivity, $\sigma^{(3)}$, can be exploited towards Kerr OFC generation in a PIC-WRR. This is accomplished by nanophotonic

---

Received 30 July 2024; revised 6 January 2025; accepted 17 February 2025. Date of publication 26 February 2025; date of current version 24 March 2025. This work was supported by the Hellenic Foundation for Research and Innovation (H.F.R.I.) through the "First Call for H.F.R.I. Research Projects to Support Faculty Members and Researchers and the Procurement of High-Cost Research Equipment Grant" under Project HFRI-FM17-2086. *(Corresponding author: Alexandros Pitilakis.)*

The authors are with the School of Electrical and Computer Engineering, Aristotle University of Thessaloniki, 541 24 Thessaloniki, Greece (e-mail: alexpiti@auth.gr; mkriezis@auth.gr).

Color versions of one or more figures in this article are available at https://doi.org/10.1109/JQE.2025.3546142.

Digital Object Identifier 10.1109/JQE.2025.3546142

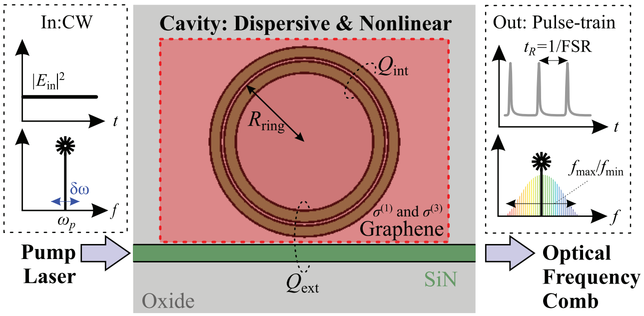

Fig. 1. Conceptual depiction of the integrated graphene-comprising configuration that can produce a Kerr OFC when pumped by a CW laser; the effective circumference of dispersive nonlinear cavity is $L = 2\pi R$.

waveguide engineering in the low-loss silicon-nitride-on-insulator (SNOI) platform, while rigorously accounting for the spectral dispersion in graphene's properties, including the nonlinearity. Note that, in contrast to typical crystals with self-focusing nonlinearity, graphene exhibits defocusing nonlinearity in the selected regime, so a normal-dispersion slot waveguide was used for phase-locked cavity soliton generation. Moreover, previous related works, e.g., [28], only employed graphene's linear surface conductivity, $\sigma^{(1)}$, to balance the overall dispersion against the bulk material-induced nonlinear phase. The encouraging results presented in this work tug towards another degree of control over the microcomb, through graphene's chemical potential (μ_c): This property can be electrically tuned by gate biasing, in a wide range [21], [32], that instantaneously modifies graphene's linear *and* nonlinear properties. Finally, another unveiled path is towards accessing graphene's rich nonlinear response at higher optical intensities: The non-perturbative regime [33], [34], [35], where photogenerated carrier-induced nonlinear refraction coincides with saturable absorption (SA) [27], can potentially further improve the Kerr microcomb performance owing to the simultaneous increase in the parametric gain and decrease in the losses (increase in Q-factor).

The structure of the paper is as follows: Following this introduction, in Section II we present the methods used in the theoretical and numerical treatment of the subject. The results are presented and analyzed in Section III and the summary and conclusions of the work can be found in Section IV.

II. METHODS

The study of Kerr microcombs in this work starts from the presentation and development of the theoretical and computational tools for the numerical simulation and proceeds to the identification of the various operational regimes and the corresponding threshold parameter ranges. We use the Lugiato-Lefever equation (LLE) framework [36], whose parameters are rigorously derived by a full-vector finite-element method (FEM) eigenmode solver applied to the ring waveguide cross-section, Fig. 2, [37]. The numerical solution of the LLE is done using split-step Fourier method (SSFM) [38], modified for the inclusion of fully dispersive linear and nonlinear properties of the waveguide and resonator system. The ultrawideband frequency dispersion of graphene properties, both linear and nonlinear, which are fed to our FEM solver, are computed using well established equilibrium quantum formulas [24], [39], [40].

A. The Lugiato-Lefever Equation Framework

Even though the LLE was first proposed [41] for the study of the interplay of FWM with diffraction in *transverse* (lateral) profiles arising in nonlinear cavities, the same equation can be used for the study of interplay between FWM and dispersion in *longitudinal* profiles [42]; the LLE equation can be easily derived from the infinite Ikeda map [43] describing the pumped nonlinear system in a ring cavity. For our purposes, the LLE provides a simple and elegant one-equation framework that allows for the full treatment of Kerr microcombs [36], [44], [45], both in the transient/dynamic and in the static regime; the former is crucial for practical "locking" to the soliton operation regime while the latter is insightful for the identification of the parameter ranges defining each operation regime. Finally, another advantage of the LLE, from the implementation perspective, is that it is essentially a damped, detuned and driven version of the nonlinear Schrödinger equation (NLSE), which have been extensively employed in straight waveguide nonlinear applications, from fibers [46] to integrated waveguides [47], and recently in increasingly more advanced formulations [27]. The alternative approach to the LLE, for the study of Kerr microcombs, is a coupled-mode theory (CMT) framework in the time domain [48], where the field in the resonator is expanded in the spectrum of its eigenmodes, which are nonlinearly coupled via FWM. It has been shown that the two approaches, LLE and CMT, are equivalent under certain approximations and can both benefit from computations in the spectral domain via FFT formulations [49].

The most widely used form of the LLE is in the two-timescales format: A slow-timeframe (t), corresponding to the evolution in the order of the round-trip time (t_R) in the travelling-wave resonator, and a fast-timeframe (τ), corresponding to the intracavity evolution and assumed to be moving with the group-velocity of the pumped resonance. The fast-time can be defined either in the interval $\tau = [-t_R/2, +t_R/2)$ or $[0, t_R)$, which can be mapped to the azimuth angle scanning the resonator circumference $\phi_R = [0, 2\pi)$, or as the reciprocal of the resonance frequencies in the band considered. We have opted for the former, as it provides a solid connection to the CMT framework and to the dispersive properties of the eigenmodes in a broad spectrum. The cavity is pumped by an external CW laser at frequency ω_p tuned near the 'closest cold-cavity resonance' (CCCR) natural frequency; the detuning of the pump laser from the CCCR frequency is defined as $\delta\omega = \omega_p - \omega_{\rm CCCR}$. For this configuration, the LLE-like equation for the study of a Kerr microcomb in the two-timescale format can be written following standard notation, e.g., see section 5.2 and Eq. (50) in [3] or Eq. (3) in [36], as

$$t_R \frac{\partial E(t,\tau)}{\partial t} = \left(L\mathcal{F}_{\rm NLSE} - \frac{\theta}{2} - i\delta_0 \right) E(t,\tau) + \sqrt{\theta} E_{\rm in}, \quad (1)$$

where $\mathcal{F}_{\mathrm{NLSE}}$ denotes an NLSE-like operator in [1/m] units

$$\mathcal{F}_{\mathrm{NLSE}} = -\frac{\alpha}{2} + i\sum_{n\geq 2}\frac{\beta_n}{n!}\left(i\frac{\partial}{\partial\tau}\right)^n + i\gamma|E|^2, \tag{2}$$

using the $\exp(+i\omega t)$ sign convention throughout. The various parameters and variables appearing in Eq. (1) and Eq. (2) are defined as follows:

- $E(t,\tau)$ is the E-field amplitude inside the resonator (i.e., along the fast-time τ) as the slow-time (t) progresses, normalized so that $|E|^2$ measures the power in Watts.
- L is the effective cavity length, e.g., $L = 2\pi R$ for a ring microresonator of radius R.
- t_R is the round-trip time and corresponds to the inverse of the FSR of the comb. It can be computed as $t_R = (Ln_{\mathrm{gr},0})/c_0$, with $n_{\mathrm{gr},0}$ being the group index at the central resonance frequency of the cavity, which is typically the CCCR frequency, $n_{\mathrm{gr},0} = n_{\mathrm{gr}}(\omega_{\mathrm{CCCR}}) \approx n_{\mathrm{gr}}(\omega_p)$.
- α in [1/m] units is the propagation power-loss coefficient of the waveguide that makes up the cavity; in resonator terms, it accounts for its intrinsic (resistive/dissipative and radiative) linewidth or Q-factor, via $\alpha L Q_{\mathrm{int}} = t_R\omega_p$.
- β_n, with $n \geq 2$, are the dispersion parameters of the waveguide, with β_2 corresponding to GVD in [s^2/m] units. When β_3 and higher are omitted, the equation is identical to the LLE. $\beta_1 = n_{\mathrm{gr}}/c_0$ is related to the t_R.
- γ is the nonlinear parameter of the waveguide in [1/m/W] units, identical to the one appearing in the NLSE.
- θ is the power coupling coefficient of the cavity, related to its external Q-factor by $Q_{\mathrm{ext}} = t_R\omega_p/\theta$. The resonator is typically designed for critical coupling, i.e., $Q_{\mathrm{ext}} \approx Q_{\mathrm{int}}$, in a wide spectral band around the ω_{CCCR}.
- $\delta_0 = \delta_0(t)$ is the normalized phase detuning of the pump with respect to the CCCR, $\delta_0 = [\beta_0(\omega_{\mathrm{CCCR}}) - \beta_0(\omega_p)]L$, where $\beta_0 = n_{\mathrm{eff}}k_0$ is the phase constant. As pumping is in the close vicinity of ω_{CCCR}, $\delta_0 \propto -\delta\omega$.
- $E_{\mathrm{in}} = E_{\mathrm{in}}(t)$ is the pumped CW E-field amplitude, with $|E_{\mathrm{in}}|^2$ measured in Watts.

In the simplest form of the above LLE-like main equation, all the parameters are constants and only the GVD parameter is considered (i.e., $\beta_n = 0$ for $n \geq 3$), in which case the main equation corresponds exactly to the original LLE [42]. However, extensions can be devised, first and foremost to include higher order dispersion (arbitrarily high), secondly, to introduce frequency dispersion to some of the parameters (e.g., to Q-factors or nonlinear coefficient, γ), thirdly, to slowly modulate the pump field, $E_{\mathrm{in}} \rightarrow E_{\mathrm{in}}(t)$, in frequency and/or amplitude, or, finally, to add more pumping lasers (colors).

In this work, we have considered the frequency dispersion of all waveguide mode parameters: α (attenuation), β (phase), and γ (nonlinear refraction parameter), Fig. 2. The parameters correspond to non-trivial waveguide eigenmode properties and thus need to be computed in a rigorous manner. We use a FEM-based full-vector waveguide mode solver [25], [37]: first we incorporate all constituting *material* dispersion (e.g., for silicon nitride, oxide, and graphene), and compute the linear modal properties in a wide spectrum, $\tilde{\alpha}(\omega)$ and $\tilde{\beta}(\omega)$, along with the corresponding mode profiles in the waveguide cross-section $\mathbf{E}(x,y)$; the profiles are then overlapped in a post-processing computation with the bulk and sheet medium self-acting nonlinear properties, $\tilde{\chi}^{(3)}_{\mathrm{Kerr}}(\omega)$ and $\tilde{\sigma}^{(3)}_{\mathrm{Kerr}}(\omega)$, respectively, to extract the nonlinear parameter $\tilde{\gamma}(\omega)$ of the mode in the whole spectrum, based on perturbation theory [25], [37]. The FEM mode solver-based analysis and optimization of the graphene-clad slot waveguide can be found in our previous works [26], [27]; here, it is crucial to point out that (i) the waveguide supports a horizontally polarized quasi-TE mode highly confined in the air-slot formed between the two high-index rails so that it maximally interacts with graphene and, (ii) the presence of graphene has minimal effect on waveguiding in the NIR band, but it can drastically tune the mode losses and nonlinearity. Following standard practice, all dispersive parameter $\{\alpha,\beta,\gamma\}$ spectra were computed on an appropriately wide span of cold-cavity resonances identified by normalized integer order, for example $\mu = [-100,+100]$, with $\mu = 0$ being the pumped CCCR; for more details see, e.g., Section II of Supplementary Information to [45] or the pyLLE software in [50].

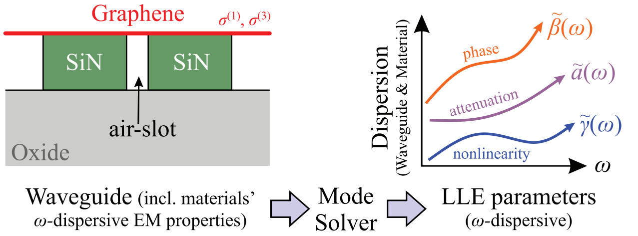

Fig. 2. Cross-section of the graphene-clad SiN-slot waveguide from which the dispersive LLE properties are rigorously extracted.

B. Applying the Split-Step Fourier Method

The numerical solution of the transient two-timescale ‘mean fields’ LLE equation can be done with the SSFM [38], [46], similarly to the NLSE, with the difference that the space-stepping is now replaced with the slow-time-stepping. The SSFM procedure involves incrementing the slow time t by a step Δt (whose appropriately chosen size is typically in the order of the round-trip time, t_R), and calculating the fast-time form of the total E-field inside the resonator at that slow-time instant, i.e., $E(t_{\mathrm{init}} + \Delta t, \tau)$. The calculation involves operations in the fast-time domain and in the spectral/frequency domain (the reciprocal of the fast-time), which are interrelated by the periodicity of the Fourier transform in these traveling wave resonators, $E(\tau) \leftrightarrow \tilde{E}(\omega)$. The initial intracavity field, i.e., $E(t_{\mathrm{init}}, \tau)$, is noise-seeded by vacuum fluctuations. Externally controlled parameters of the modeled system, e.g., the pump frequency (detuning) or power, can be changed along the slow-time. Finally, the total power of the comb, i.e., the sum of power in all spectral lines, and the out-coupled fields can be computed at each slow-time instant from $E(t,\tau)$, the field inside the resonator.

In our implementation, the spectral domain corresponds to the azimuthal-mode resonance orders relative to the pumped resonance (e.g., to the integers $\mu = [-100,+100]$, with

$\mu = 0$ being the pumped CCCR), and not to a set of equidistant spectral frequencies. The effect of the linear dispersive terms, i.e., $\{\alpha, \beta, \gamma, \theta\}$ in Eq. (1) and (2), are directly introduced in the spectral (ω_μ or just μ) domain using discrete Fourier transform of the fast-time fields; this approach has been proven [49] to be equivalent to CMT approaches [48] but more computationally efficient than performing all operations in the time domain. The dispersion of the modal attenuation constant, $\tilde{\alpha}(\omega)$, that is relevant to this work, is directly introduced as an imaginary part in the real-valued phase constant, $\tilde{\beta}(\omega)$. This approach is far superior to time-derivatives, e.g., Section 2.3.2 in [46], from the numerical implementation standpoint; moreover, it allows us to consider an arbitrary order of terms, much how it is standard practice for the phase dispersion.

The effect of the instantaneous nonlinear terms is introduced to the intracavity E-fields in the fast-time (τ) domain, by a slow-time stepping algorithm, i.e., in an averaged/mean-fields sense [42]. The slow-time step size Δt can be adaptively adjusted along the simulation, with respect to the overall magnitude of the nonlinearity and the intracavity power, balancing the trade-off between computational efficiency and accuracy; in terms of the perturbation theory, the criterion to satisfy is that the peak accumulated phase due to nonlinear refraction is vanishingly small,

$$\Delta\Phi_{\mathrm{NL}} = \gamma P_{\mathrm{peak}} \Delta z' \ll 1, \tag{3}$$

where $P_{\mathrm{peak}} = \max_\tau\{|E(t,\tau)|^2\}$ and $z' = (L/t_R)t$, in [m] units, is the distance traveled along the resonator circumference at the mean group velocity as slow-time advances. Now, the dispersion of the nonlinear mode parameter, $\tilde{\gamma}(\omega)$, is introduced as follows: Considering only the last term in Eq. (2), plugged into Eq. (1) with everything else zeroed out, we write $\partial E/\partial z' = +i\gamma |E|^2 E = \hat{N}_\gamma E$; the nonlinear τ-domain operator can be formally written using the $\tilde{\gamma}$ spectra and fast-time field $E = E(\tau)$ as

$$\hat{N}_\gamma = +i\frac{\mathrm{IFT}\left\{\tilde{\gamma}(\omega)\,\mathrm{FT}\left\{|E|^2 E\right\}\right\}}{E} \tag{4}$$

in [1/m] units, where FT/IFT is the forward/inverse Fourier transform pair. In the standard perturbation practice, the fast-time field after a nonlinear step $\Delta z' = (L/t_R)\Delta t$ can be written as

$$\frac{\partial E}{\partial z'} = \hat{N}_\gamma E \Rightarrow E(z' + \Delta z', \tau) \approx E(z', \tau)\exp(\hat{N}_\gamma \Delta z'). \tag{5}$$

Finally, an iterative Crank-Nicolson (CN)-like numerical scheme is also employed to increase the step size with controlled error; it involves a fictitious mid-step and the consequent splitting of the linear and nonlinear contributions in two halves. Typically, 2-5 CN iterations are enough for $\Delta\Phi_{\mathrm{NL}} \approx 0.1$ rad.

Summarizing the SSFM algorithm for the solution of the LLE: Knowing the ‘step-start’ E-field inside the resonator, i.e., $E(t_{\mathrm{start}}, \tau)$, the following procedures take place for each slow-time step Δt, i.e., to compute the ‘step-end’ field $E(t_{\mathrm{end}}, \tau)$:

1) Adjust any external t-dependent parameters (e.g., δ_0 for scanning the pump laser detuning through the ω_{CCCR}).
2) Compute maximum step-size Δt using Eq. (3).
3) Add in-coupled pump, $\sqrt{\theta}E_{\mathrm{in}}$ in Eq. (1) in τ-domain; if θ is dispersive, add in ω_μ-domain using FT/IFT pair.
4) Add dispersive linear and nonlinear term contributions in the ω_μ- and τ-domains, respectively, as explained above.
5) Perform CN iterations until $E(t_{\mathrm{end}}, \tau)$ converges.
6) Compute comb power and out-coupled spectra.

C. Identifying Operation Regimes and Critical Parameters

The pumped nonlinear/dispersive resonator system provides a rich platform for nonlinear dynamics, of which the phase-locked cavity soliton is one possible regime. These dynamics can be studied via the steady-state solutions of the LLE, derived by negating the slow-time derivative and, optionally, also the fast-time derivative. Without going into details that pertain to the bifurcations of the nonlinear system [51], we will say that the parameters that mostly govern its response are the CW pumping power, $|E_{\mathrm{in}}|^2$, the pump frequency detuning, $\delta\omega$, and the GVD, β_2; note that the sign relation between $\{\delta\omega, \beta_2, \gamma\}$ also defines the operation regime. For instance, for bright solitons to arise, a combination of self-focusing nonlinearity (positive γ) and anomalous GVD (negative β_2) is typically used; however, the same dynamics can be attained for opposite-sign parameter values, i.e., for defocusing nonlinearity (negative γ) with normal GVD (positive β_2).

The relevant conclusions extracted from such a stability analysis are the following: (i) there is always, i.e., for any detuning, a laser power range in which a Kerr comb can be generated, and (ii) there is an optimal path to traverse the LLE-solution bifurcation map to lock-in to a stable Kerr comb. Building upon the latter conclusion, the detuning of the pump laser frequency with respect to the CCCR is both one of the critical parameters for a Kerr microcomb and one that can be easily controlled (externally); so it is immensely important. Typically, the detuning is temporally scanned (specifically by slowly de/increasing the pump frequency through the main resonance, for anomalous/normal GVD regime, respectively) to lock into a stable cavity soliton regime, whose spectrum corresponds to a wideband comb.

The four characteristic operation regimes, for the most often used case of {positive γ; anomalous GVD; CW pump} can be successively attained for pump frequency *decreasing* through the CCCR (starting from $\omega_p > \omega_{\mathrm{CCCR}}$, i.e., $\delta\omega > 0$):

1) **Modulation Instability** (MI) induced stable dissipative structures in the τ-domain, also referred to as “Turing rolls”; the spectrum is a primary comb with teeth spaced by several FSRs and is attained for $\delta\omega > 0$ or near-zero.
2) **MI-induced chaos**, i.e., unstable dissipative structures with a broad but noisy spectrum centered at ω_p; this regime typically arises for slightly negative $\delta\omega$.
3) **Soliton breathers** (or molecules), i.e., multiple unstable dissipative cavity solitons that rapidly evolve (e.g., shift, split, merge, collide or even disappear) as t advances; this transitional regime is typically ‘brief’ in $\delta\omega$ tuning.
4) **Phase-locked stable cavity soliton(s)**, one or multiple, with narrow hyperbolic secant pulse shapes corresponding to a well-formed broadband comb-like spectrum; this regime is largely stable, and the soliton phase and amplitude can be mildly tuned for a broad $\delta\omega < 0$ range.

For larger detuning, above or below the CCCR frequency, the CW laser cannot efficiently couple power into the resonator and, thus, there are no temporal dynamics (output is CW).

The CW pumping power required for stable cavity solitons to emerge (wide-span OFC) has both upper and lower limits; we are interested in minimizing the lower threshold. It can be shown that the power is proportional to the normalized parameter F^2, where F is defined in Eq. (7) of [51]; under the assumption of critical coupling and $n_{\mathrm{eff}} \approx n_{\mathrm{gr},0}$, the estimated threshold power can be written in terms of the quantities defined in this work as

$$F^2 \approx \frac{|\gamma|}{L\alpha^2}|E_{\mathrm{in}}|^2. \tag{6}$$

Threshold values for primary comb (Turing rolls) formation are in the order of $F^2 \approx 2$ but, depending on dispersion, realistic full combs require two or four times that power. In all cases, low waveguide losses (high Q_{int}), high nonlinearity, and short cavities help decrease the pumping power threshold. However, note that, in integrated micro-resonators, L cannot be decreased too much, because bending (radiative) losses would become significant and add to the ohmic (resistive) losses for which the modal attenuation α primarily accounts for in this work.

D. Electro-Optical Control via Graphene

We assume that a graphene monolayer sheet is covering an integrated WRR in such a way that the lightwave travelling along the waveguide can maximally interact with it. Appropriately designed electrical contacts are assumed integrated in the structure, e.g., [21], [28], [32], and [33], without interfering with the optical propagation, so that graphene's optical response can be tuned practically instantaneously and with only a few-V voltage. In quantum electronic terms, tuning refers to a change in graphene's chemical potential (μ_c), or Fermi energy, exploiting its linear energy-momentum dispersion and the zero-bandgap feature, valid near the tip of the Dirac cone [18]. Theoretical and experimental evidence for linear and third-order nonlinear surface conductivity, $\sigma^{(1)}$ and $\sigma^{(3)}$, respectively, confirm the importance of tuning μ_c with respect to the *half-photon energy*, i.e., $\mu_c \lesseqgtr \hbar\omega/2$.

In the NIR spectrum, pristine graphene ($|\mu_c| \ll \hbar\omega/2$) is quite absorptive despite its atomic thickness: its linear conductivity takes the characteristic value $\sigma^{(1)} \approx \sigma_0 \equiv q^2/4\hbar \approx 61\ \mu$S, responsible for the 2.3% absorption by a free-standing monolayer at normal incidence. Tuning so that $|\mu_c| > \hbar\omega/2$ cancels the interband absorption mechanism (Pauli blocking) and thus reduces graphene absorption making it optically transparent, $|\sigma^{(1)}| \ll \sigma_0$. The spectra $\tilde{\sigma}^{(1)}(\omega)$ can be computed by the Kubo-formulas [24], [39] and depend, apart from μ_c, also on the ambient temperature and quality of graphene sample; the latter is usually quantified by the intraband and interband momentum relaxation lifetimes (τ_i and τ_e, respectively) or the corresponding carrier mobilities. Note that the $\mathrm{Im}\{\tilde{\sigma}^{(1)}\}$, contributing to the phase constant, can also be electrically controlled and exhibits a sharp resonance (maximization) near $\mu_c = \hbar\omega/2$; this property was used in [28] to tune the dispersion of the Kerr comb.

The third-order Kerr-like perturbative nonlinearity of graphene in the NIR, both its magnitude and its sign, have been a topic of much debate over the last 15 years [52]. The present consensus is that graphene's NIR nonlinearity near $\mu_c = \hbar\omega/2$ is *defocusing* with a peak in its magnitude, which is appreciable, e.g., $\sigma^{(3)}_{\mathrm{Kerr}} \approx +i10^{-21}$ S(m/V)^2. The actual value and sign can vary, especially with respect to $2\mu_c/\hbar\omega$, while some rather involved expressions for the complex-valued $\tilde{\sigma}^{(3)}(\omega)$ spectra have been extracted by quantum calculations at equilibrium [24], [39], which have been implemented in MATLAB code [40]. Note that by $\sigma^{(3)}_{\mathrm{Kerr}}$ we refer to the 'self-acting' nonlinearity, i.e., the response of the medium onto itself when illuminated by monochromatic radiation at ω. Formally, we write $\sigma^{(3)}_{\mathrm{Kerr}}$ as a fourth-rank tensor [24], [39], $\sigma^{(3)}_{d;abc}(-\omega,\omega,\omega)$ with $\{a,b,c,d\} = \{x,y,z\}$ being the components of the E-field; symmetries can be used to greatly simplify it, eventually revealing that only one tensor component, e.g., $\sigma^{(3)}_{x;xxx}$, is enough to fully quantify graphene's Kerr response for the in-plane arrangement depicted in Fig. 2.

It is worth pointing out that $\mathrm{Im}\{\tilde{\sigma}^{(3)}\}$ corresponds to the Kerr effect, i.e. refractive nonlinearity, while $\mathrm{Re}\{\tilde{\sigma}^{(3)}\}$, which can also be non-zero, denotes induced transparency (saturable absorption or photo-bleaching) or induced absorption (similar to two-photon absorption), depending on its sign. Finally, we stress that for high effective optical intensities, e.g., above 10 MW/cm^2, graphene nonlinearity enters into a non-perturbative electrodynamic regime where more complicated transient effects arise [32], [53]; of particular interest is high photogenerated carrier nonlinear refraction and deep saturable absorption [27], [33], [34].

III. RESULTS

Our aim is to showcase the potential of Kerr microcomb generation in integrated waveguide ring resonators operating near the telecom wavelength of $\lambda_0 = 1550$ nm (193.4 THz). To achieve a full-octave span we need to study the spectral band between $[0.75,1.5]\lambda_0$ which is [2.33,1.16] μm in our case, i.e., spanning 130 THz (130-260 THz). Most importantly, the lower wavelength is very close to silicon's bandgap, where absorption will be detrimental. Thus, the integrated platform of choice in this work is Si$_3$N$_4$-on-insulator (SNOI), where foundry technology enables very low losses and high geometric feature resolution. The latter is important because graphene's maximum nonlinearity in this band is defocusing ($\gamma < 0$), meaning that our waveguide must have normal GVD for bright solitons to emerge. Now, normal GVD can be attained by the slot waveguide archetype (wire/rib type waveguides have anomalous dispersion), where waveguide engineering [26] has shown that a sufficiently narrow spacing between the two rails, e.g., 50 nm, is required to maximize the TE-polarized mode-field confinement in the slot and on the graphene sheet, which leads to a maximal $|\gamma|$. In this work, the refractive index of Si$_3$N$_4$ is taken by Sellmeier-like formulas of [54] with a value of 1.98 at 1550 nm; for its nonlinear index, we assume a flat value of $n_2 = +2.4 \times 10^{-19}$ m^2/W (the plus sign denotes a self-focusing nonlinearity); of course, we note that in real-world conditions, the index of stoichiometric Si$_3$N$_4$

can easily vary at the second or even first decimal depending on the growth conditions and process (LP-CVD vs. PE-CVD).

Concerning graphene, an unpatterned monolayer is employed in this work, assumed to fully clad the SNOI waveguides, Fig. 2. As described in the Methods, Section II-D, its relevant electromagnetic properties are: (i) $\tilde{\sigma}^{(1)}(\omega;\mu_c,T,\tau_{i,e})$, used by the FEM waveguide solver to compute the phase and attenuation spectra, and (ii) $\tilde{\sigma}^{(3)}(\omega;\mu_c,T,\tau_{i,e})$, used in a post-processing of the transverse waveguide mode profile to compute the self-acting Kerr nonlinear parameter spectra. In this work, we used the formulas of [24][1] with a lattice temperature of 300 K and assuming good quality graphene samples, corresponding to intra- and interband momentum relaxation lifetimes of $\tau_{i,e} = 20$ fs (equivalent rates $\Gamma_{i,e} = 33$ meV). It is worth stressing that no other loss mechanisms, e.g., bending loss or scattering from sidewall roughness or intrinsic absorption in the dielectrics (e.g., $\tan\delta$ or imaginary part in the refractive index), are considered in this work, because the linear graphene conductivity $\mathrm{Re}\{\tilde{\sigma}^{(1)}\}$ vastly dominates in these highly-confining nanophotonic waveguides.

A. Preliminary Dispersionless Case

We start from a preliminary dispersionless case study, where only the key LLE parameters have been introduced, using spectrum-averaged values. We consider a SNOI-slot waveguide ring resonator made of two SiN rails of $1\mu\text{m}\times0.5\mu\text{m}$ spaced by 50 nm and clad by a graphene monolayer, Fig. 2, with a constant linear conductivity $\sigma^{(1)}$ for $\mu_c > \hbar\omega/2$ (corresponding to the low-loss regime) and a constant dispersionless nonlinear surface conductivity of $\sigma^{(3)} = +i10^{-21}$ [S(m/V)^2], purely imaginary with the positive sign corresponding to defocusing refraction. The ring-resonator radius was chosen so that its circumference is $L = 100$ μm. From these, we calculate the LLE parameters at the pumping wavelength of 1550 nm (193.4 THz): $n_{\mathrm{gr},0} \approx 2$ (FSR is 1.5 THz and roundtrip time is 0.67 ps), $\alpha = 0.8$/mm ($Q_{\mathrm{int}} \approx 10^4$), $\gamma \approx -100$ m^{-1}W^{-1}, $\beta_2 = +1.1$ ps^2/m, and $\beta_3 = -0.0025$ ps^3/m. Assuming critical coupling ($Q_{\mathrm{ext}} = Q_{\mathrm{int}}$) at the central frequency, Eq. (6) gives a 1.3 W threshold for $F^2 = 2$, but a 5 W pumping power is required to produce an appreciable and stable Kerr comb; this was numerically verified in Fig. 3, by scanning the pump-laser detuning from −50 to 200 GHz ($\delta_0 = +2.6$ to -10.5). This configuration produces a comb with a 60 dB span from 120 to 270 THz [Fig. 3(b) near $t = 12.5$ ns] corresponding to 125% octave. We stress that the four characteristic regimes (Turing rolls, MI-chaos, soliton breather, phase-locked soliton) are now observed as the pump frequency is *increased* through the resonance, coming to a bright soliton for $\delta_0 < 0$ ($\delta\omega > 0$); this is opposite from the regular case of anomalous β_2 and self-focusing γ, where the bright soliton regime emerges for $\delta_0 > 0$ ($\delta\omega < 0$). We also note that the produced soliton, albeit stable for a large detuning range, is quite dispersive as denoted by the diagonal traces in Fig. 3(a) between 7 and 12.5 ns, owing to the high GVD and TOD. This preliminary case study helps us gain confidence that graphene can indeed produce Kerr microcombs, albeit at high pump power,[2] but with the same features as the ones observed in more well understood configurations. Our next goal is to assess whether the high dispersion in graphene nonlinearity can detrimentally affect Kerr OFC generation.

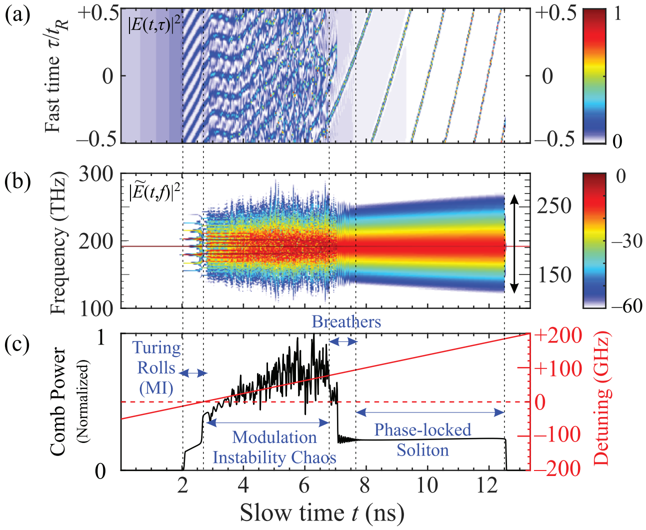

Fig. 3. A FSR ≈ 1.5 THz Kerr microcomb produced by 5 W pumping of a simplified graphene-clad SNOI-slot WRR. Evolution of normalized intracavity (a) fast-time field $|E(t,\tau/t_R)|^2$, (b) spectrum $|\tilde{E}(t,f)|^2$ in dB, and (c) total comb power, as the pump frequency is linearly ramped with slow-time (t) passage. Spectrally-averaged LLE parameters: $n_{\mathrm{gr},0} \approx 2$, $L = 100$ μm, $\alpha = 0.8$/mm ($Q_{\mathrm{int}} \approx 10^4$), $\beta_2 = +1.1$ ps^2/m, $\beta_3 = -0.0025$ ps^3/m, $\gamma = -100$ m^{-1}W^{-1}, $Q_{\mathrm{ext}} = Q_{\mathrm{int}}$.

B. Full Waveguide Dispersion

The $\sigma^{(1)}$ and $\sigma^{(3)}$ values chosen for graphene in the previous case-study were optimistic and dispersionless, as evidenced by the symmetric spectra in Fig. 3(b). We take a step towards more realistic modeling by including the dispersion of all waveguide parameters in the LLE. We use quantum-electronic theory predicted formulas for graphene's $\tilde{\sigma}^{(1)}$ and $\tilde{\sigma}^{(3)}$ [24], [40], which dominate the dispersion of the waveguide losses (α or Q_{int}) and nonlinear parameter (γ), respectively. As previously mentioned, no other loss mechanisms apart from $\mathrm{Re}\{\tilde{\sigma}^{(1)}\}$ are considered in this work, being negligible compared to graphene losses. Note that, for this waveguide, the phase dispersion (i.e., the parameters β_n, $n \geq 2$) is dominated by the waveguide and bulk SNOI material dispersion, and not by graphene's $\mathrm{Im}\{\sigma^{(1)}\}$ dispersion.

To assess the magnitude of the dispersion, we sweep graphene's chemical potential (μ_c) and extract the spectra of the waveguide parameters with a mode solver, Fig. 2, seeking optimum configurations for an octave span around the central pumping at 1550 nm; for this study, the SiN rail width was reduced to 800 nm. The resulting parameter spectra are depicted in Fig. 4, where we observe graphene's well-known trade-off between low losses and high nonlinearity near the

---

[1] For $\sigma^{(1)}$, Eq. (11)-(12) and (B1); for $\sigma^{(3)}$, Eq. (14)-(26) and (34). These formulas have been implemented in MATLAB code by the Authors [40].

[2] Breathing solitons could be produced for lower pumping powers, e.g., 2.5-3 W, but a very careful laser scanning was required.

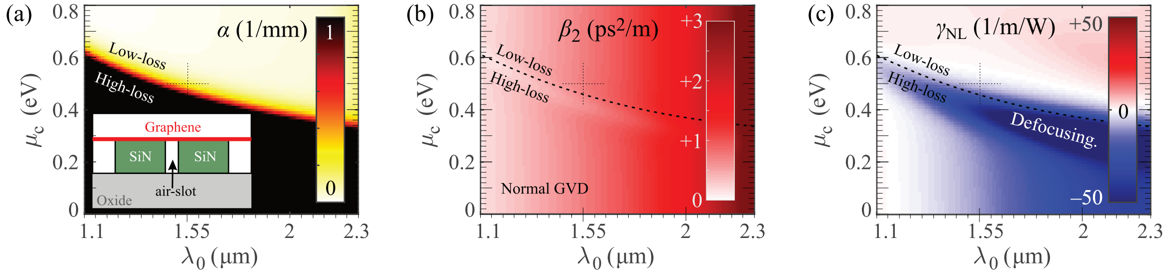

Fig. 4. Frequency and μ_c dispersion of the waveguide parameters that are introduced in the LLE: (a) attenuation, (b) GVD, and (c) nonlinear parameter. The slot waveguide is made of two 800 nm×500 nm SiN rails spaced by 50 nm and overlaid by a good quality graphene monolayer ($\tau_{i,e}$ = 20 fs) at room temperature [40]. The dotted cross marks the selected μ_c and pump wavelength.

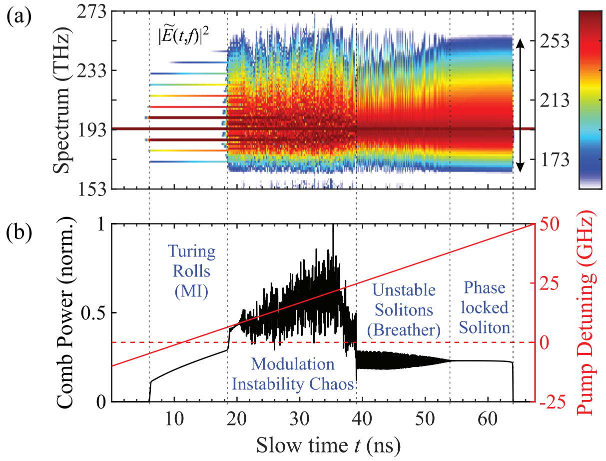

Fig. 5. The evolution of the 1.48 THz-FSR comb's intracavity (a) spectrum and (b) total power, as the pump detuning is slowly swept through the 1550 nm resonance. The pumping power is 10 W and the full wideband dispersion of all parameters is accounted for as explained in the text.

half-photon energy line, in panels (a) and (c); in panel (b), we note that GVD is lower in the same region, which is favorable for more stable solitons, and is normal in all studied regions. The higher order phase dispersion parameters, β_n for $n \geq 3$, are extracted by numerical differentiation of the $n_{\text{eff}}(\omega)$ spectra computed by the mode solver. Finally, we note that the dispersion of the coupling coefficient θ was not considered in this work, i.e., a constant Q_{ext} was selected, for critical coupling on the main resonance; engineering of the coupling section between the access and ring waveguide, Fig. 1, requires more rigorous analysis, to ensure broadband matching of the two Q-factors.

Now, to evaluate the performance of this more realistic Kerr comb, we choose $\mu_c = 0.5$ eV as a compromise between low losses and adequately negative (defocusing) nonlinearity. We perform an LLE simulation with the SSFM with a higher CW pump power, 10 W, to compensate for the lower nonlinear parameter; we sweep the pump detuning from −10 to +50 GHz, acquiring the comb depicted in Fig. 5. The 60 dB bandwidth spans from 165 to 255 THz (55% octave), i.e., is less than half of what was attained in the optimistic dispersionless case. The spectra are naturally asymmetric, and we note a higher efficiency towards the blue flank, i.e., to the region where γ remains negative despite the increase of the losses; the red flank of the comb spectrum is more suppressed owing to the reduction of γ, Fig. 4(c).

C. Further Improvement

Revisiting Eq. (6), where the figure-of-merit $F^2 \propto \gamma/\alpha^2$ minimizes the pumping power for given cavity length L, we apply a spectral weighting on the (λ_0, μ_c)-dependent heatmaps of Fig. 4(a) and (c). From these, we infer that a two-fold decrease in $|E_{\text{in}}|^2$ could be achieved by pumping near $\lambda_0 \approx 1.95$ μm with graphene tuned at $\mu_c \approx 0.43$ eV.

Additionally, the SNOI waveguide dimensions could be re-engineered to seek an optimal combination between $\{\alpha, \beta_2, \gamma\}$ or one could investigate graphene's aspects, e.g., the region $\mu_c > \hbar\omega$ where its nonlinearity is self-focusing (with wire-type waveguide) or what improvement is attained for higher quality samples ($\tau_{i,e} > 20$ fs).

Finally, we could probe graphene's richer nonlinear photoconductivity when it is pumped into the non-equilibrium thermodynamic regime where, apart from thermal effects, we must also consider the photogenerated carrier temporal dynamics, which are in the order of the roundtrip time. In such a regime, the combination of nonlinear refraction and saturable absorption [27], corresponding to higher γ and Q, respectively, offer an ideal combination for enhanced performance in Kerr comb generation. Experimental evidence of this regime are limited [34] but there are encouraging perspectives to explore [52].

IV. SUMMARY AND OUTLOOK

We have theoretically and numerically demonstrated that graphene's own third-order nonlinearity can be used to produce voltage-controlled octave-spanning THz-wide FSR Kerr microcombs, when a simple monolayer clads an engineered silicon-nitride slot-waveguide ring resonator. The analysis was carried out using the Lugiato-Lefever equation framework, which was modified to include the ultra-wideband frequency dispersion of all underlying waveguide parameters, including the all-important nonlinearity. For the numerical extraction of the LLE parameters in a broad band, we utilized a rigorous full-vector mode-solver formulation, fed by graphene's dispersive linear and nonlinear surface conductivities; the latter were computed by perturbatively-extracted quantum-electronic formulas at thermal equilibrium.

From a technological perspective, the problem with all graphene-comprising waveguides are the linear losses which impose a threshold on the intrinsic Q-factor of the cavity and hence increase the power threshold; note that the formulas used here predict a maximal nonlinearity-over-losses figure-of-merit when graphene is biased in the vicinity of half-photon energy, i.e., relatively close to its high-loss regime. A possible way to overcome this limitation is by pumping graphene in the non-perturbative regime [53], where the combination of saturable absorption and nonlinear refraction can prove beneficial [27]; the study of these transient free-carrier effects in a pumped cavity for OFC generation is an outstanding challenge.

In all cases, the contribution of this paper shows that graphene's voltage-tunable linear and nonlinear response can provide another degree of freedom, complementing single/multi-pump frequency detuning or amplitude modulation, for enhanced Kerr comb control [55] or parametric gain. This proof-of-concept can be exploited in other nonlinear devices, both resonator-based, e.g., mode-locked and Q-switched lasers [56], [57] and LiDAR [12], and non-resonant, e.g., supercontinuum generation or topological lattices. Finally, the LLE formulation developed here can be helpful in modeling other systems or devices characterized by pronounced and ultrawideband dispersion in their nonlinearity, such as cavities formed by metasurfaces [58].

REFERENCES

[1] Y. K. Chembo, "Kerr optical frequency combs: Theory, applications and perspectives," *Nanophotonics*, vol. 5, no. 2, pp. 214–230, Jun. 2016.

[2] T. J. Kippenberg, A. L. Gaeta, M. Lipson, and M. L. Gorodetsky, "Dissipative Kerr solitons in optical microresonators," *Science*, vol. 361, no. 6402, pp. 129–162, Aug. 2018.

[3] A. Pasquazi et al., "Micro-combs: A novel generation of optical sources," *Phys. Rep.*, vol. 729, pp. 1–81, Jan. 2018.

[4] P. Del'Haye, A. Schliesser, O. Arcizet, T. Wilken, R. Holzwarth, and T. J. Kippenberg, "Optical frequency comb generation from a monolithic microresonator," *Nature*, vol. 450, no. 7173, pp. 1214–1217, Dec. 2007.

[5] T. J. Kippenberg, R. Holzwarth, and S. A. Diddams, "Microresonator-based optical frequency combs," *Science*, vol. 332, no. 6029, pp. 555–559, Apr. 2011.

[6] A. L. Gaeta, M. Lipson, and T. J. Kippenberg, "Photonic-chip-based frequency combs," *Nature Photon.*, vol. 13, no. 3, pp. 158–169, Mar. 2019.

[7] L. Chang, S. Liu, and J. E. Bowers, "Integrated optical frequency comb technologies," *Nature Photon.*, vol. 16, no. 2, pp. 95–108, Feb. 2022.

[8] A. Rizzo et al., "Petabit-scale silicon photonic interconnects with integrated Kerr frequency combs," *IEEE J. Sel. Topics Quantum Electron.*, vol. 29, no. 1, pp. 1–20, Jan. 2023.

[9] P. Marin-Palomo et al., "Microresonator-based solitons for massively parallel coherent optical communications," *Nature*, vol. 546, no. 7657, pp. 274–279, Jun. 2017.

[10] J. Wu et al., "RF photonics: An optical Microcombs' perspective," *IEEE J. Sel. Topics Quantum Electron.*, vol. 24, no. 4, pp. 1–20, Jul. 2018.

[11] P. Trocha et al., "Ultrafast optical ranging using microresonator soliton frequency combs," *Science*, vol. 359, no. 6378, pp. 887–891, Feb. 2018.

[12] A. Lukashchuk, J. Riemensberger, A. Tusnin, J. Liu, and T. J. Kippenberg, "Chaotic microcomb-based parallel ranging," *Nature Photon.*, vol. 17, no. 9, pp. 814–821, Jul. 2023.

[13] S. B. Papp et al., "Microresonator frequency comb optical clock," *Optica*, vol. 1, no. 1, p. 10, Jul. 2014.

[14] M.-G. Suh, Q.-F. Yang, K. Y. Yang, X. Yi, and K. J. Vahala, "Microresonator soliton dual-comb spectroscopy," *Science*, vol. 354, no. 6312, pp. 600–603, Nov. 2016.

[15] W. Liang et al., "High spectral purity Kerr frequency comb radio frequency photonic oscillator," *Nature Commun.*, vol. 6, no. 1, p. 7957, Aug. 2015.

[16] D. T. Spencer et al., "An optical-frequency synthesizer using integrated photonics," *Nature*, vol. 557, no. 7703, pp. 81–85, Apr. 2018.

[17] R. A. McCracken, J. M. Charsley, and D. T. Reid, "A decade of astrocombs: Recent advances in frequency combs for astronomy," *Opt. Exp.*, vol. 25, no. 13, p. 15058, Jun. 2017.

[18] F. Bonaccorso, Z. Sun, T. Hasan, and A. C. Ferrari, "Graphene photonics and optoelectronics," *Nature Photon.*, vol. 4, no. 9, pp. 611–622, Sep. 2010.

[19] M. Liu et al., "A graphene-based broadband optical modulator," *Nature*, vol. 474, no. 7349, pp. 64–67, Jun. 2011.

[20] V. Sorianello et al., "Graphene–silicon phase modulators with gigahertz bandwidth," *Nature Photon.*, vol. 12, no. 1, pp. 40–44, Jan. 2018.

[21] T. Jiang et al., "Gate-tunable third-order nonlinear optical response of massless Dirac fermions in graphene," *Nature Photon.*, vol. 12, no. 7, pp. 430–436, May 2018.

[22] E. Hendry, P. J. Hale, J. Moger, A. K. Savchenko, and S. A. Mikhailov, "Coherent nonlinear optical response of graphene," *Phys. Rev. Lett.*, vol. 105, no. 9, Aug. 2010, Art. no. 097401.

[23] T. Gu et al., "Regenerative oscillation and four-wave mixing in graphene optoelectronics," *Nature Photon.*, vol. 6, no. 8, pp. 554–559, Aug. 2012.

[24] J. L. Cheng, N. Vermeulen, and J. E. Sipe, "Third-order nonlinearity of graphene: Effects of phenomenological relaxation and finite temperature," *Phys. Rev. B, Condens. Matter*, vol. 91, no. 23, Jun. 2015, Art. no. 235320.

[25] D. Chatzidimitriou, A. Pitilakis, and E. E. Kriezis, "Rigorous calculation of nonlinear parameters in graphene-comprising waveguides," *J. Appl. Phys.*, vol. 118, no. 2, Jul. 2015, Art. no. 023105.

[26] A. Pitilakis, D. Chatzidimitriou, T. V. Yioultsis, and E. E. Kriezis, "Asymmetric Si-slot coupler with nonreciprocal response based on graphene saturable absorption," *IEEE J. Quantum Electron.*, vol. 57, no. 3, pp. 1–10, Jun. 2021.

[27] A. Pitilakis and E. E. Kriezis, "Ultrafast pulse propagation in graphene-comprising nanophotonic waveguides considering nonperturbative electrodynamic nonlinearity," *J. Opt. Soc. Amer. B, Opt. Phys.*, vol. 39, no. 10, p. 2723, Sep. 2022.

[28] B. Yao et al., "Gate-tunable frequency combs in graphene–nitride microresonators," *Nature*, vol. 558, no. 7710, pp. 410–414, Jun. 2018.

[29] W. Chen et al., "Design of a graphene-enabled dual-mode Kerr frequency comb," *IEEE J. Sel. Topics Quantum Electron.*, vol. 28, no. 3, pp. 1–7, May 2022.

[30] P. Mondal and S. K. Selvaraja, "Nonlinear spectral broadening of a dual-carrier electro-optic frequency comb in a graphene oxide cladded silicon-rich nitride hybrid waveguide," *Appl. Opt.*, vol. 61, no. 27, p. 7852, 2022.

[31] W. Chen et al., "Theoretical analysis of a mid-infrared Kerr frequency comb in a graphene-on-silicon micro-resonator," *Phys. Scripta*, vol. 98, no. 6, Jun. 2023, Art. no. 065525.

[32] K. Alexander, N. A. Savostianova, S. A. Mikhailov, D. Van Thourhout, and B. Kuyken, "Gate-tunable nonlinear refraction and absorption in graphene-covered silicon nitride waveguides," *ACS Photon.*, vol. 5, no. 12, pp. 4944–4950, Nov. 2018.

[33] N. Vermeulen et al., "Graphene's nonlinear-optical physics revealed through exponentially growing self-phase modulation," *Nature Commun.*, vol. 9, no. 1, Jul. 2018, Art. no. 2675.

[34] P. Demongodin et al., "Ultrafast saturable absorption dynamics in hybrid graphene/Si3N4 waveguides," *APL Photon.*, vol. 4, no. 7, Jul. 2019, Art. no. 076102.

[35] D. Castelló-Lurbe, H. Thienpont, and N. Vermeulen, "Predicting graphene's nonlinear-optical refractive response for propagating pulses," *Laser Photon. Rev.*, vol. 14, no. 6, May 2020, Art. no. 1900402.

[36] S. Coen, H. G. Randle, T. Sylvestre, and M. Erkintalo, "Modeling of octave-spanning Kerr frequency combs using a generalized mean-field Lugiato–Lefever model," *Opt. Lett.*, vol. 38, no. 1, p. 37, Dec. 2012.

[37] A. Pitilakis, D. Chatzidimitriou, and E. E. Kriezis, "Theoretical and numerical modeling of linear and nonlinear propagation in graphene waveguides," *Opt. Quantum Electron.*, vol. 48, no. 4, Mar. 2016, Art. no. 243.

[38] O. V. Sinkin, R. Holzlohner, J. Zweck, and C. R. Menyuk, "Optimization of the split-step Fourier method in modeling optical-fiber communications systems," *J. Lightw. Technol.*, vol. 21, no. 1, pp. 61–68, Jan. 2003.

[39] S. A. Mikhailov, "Quantum theory of the third-order nonlinear electrodynamic effects of graphene," *Phys. Rev. B*, vol. 93, no. 8, Feb. 2016, Art. no. 085403.

[40] A. Pitilakis, "MATLAB code for calculation of perturbative third-order nonlinear surface conductivity of graphene," Zenodo, v1.00, Aristotle Univ. Thessaloniki, Thessaloniki, Greece, 2024, doi: 10.5281/zenodo.12738208. [Online]. Available: https://github.com/alexpiti/Graphene_Nonlinearity

[41] L. A. Lugiato and R. Lefever, "Spatial dissipative structures in passive optical systems," *Phys. Rev. Lett.*, vol. 58, no. 21, pp. 2209–2211, May 1987.

[42] M. Haelterman, S. Trillo, and S. Wabnitz, "Dissipative modulation instability in a nonlinear dispersive ring cavity," *Opt. Commun.*, vol. 91, nos. 5–6, pp. 401–407, Aug. 1992.

[43] K. Ikeda, "Multiple-valued stationary state and its instability of the transmitted light by a ring cavity system," *Opt. Commun.*, vol. 30, no. 2, pp. 257–261, Aug. 1979.

[44] Y. K. Chembo and C. R. Menyuk, "Spatiotemporal Lugiato-Lefever formalism for Kerr-comb generation in whispering-gallery-mode resonators," *Phys. Rev. A, Gen. Phys.*, vol. 87, no. 5, May 2013, Art. no. 053852.

[45] T. Herr et al., "Temporal solitons in optical microresonators," *Nature Photon.*, vol. 8, no. 2, pp. 145–152, Dec. 2013.

[46] G. P. Agrawal, *Nonlinear Fiber Optics*, 4th ed., New York, NY, USA: Academic, 2006.

[47] Q. Lin, O. J. Painter, and G. P. Agrawal, "Nonlinear optical phenomena in silicon waveguides: Modeling and applications," *Opt. Exp.*, vol. 15, no. 25, p. 16604, 2007.

[48] Y. K. Chembo and N. Yu, "Modal expansion approach to optical-frequency-comb generation with monolithic whispering-gallery-mode resonators," *Phys. Rev. A, Gen. Phys.*, vol. 82, no. 3, Sep. 2010, Art. no. 033801.

[49] T. Hansson, D. Modotto, and S. Wabnitz, "On the numerical simulation of Kerr frequency combs using coupled mode equations," *Opt. Commun.*, vol. 312, pp. 134–136, Feb. 2014.

[50] G. Moille, Q. Li, L. Xiyuan, and K. Srinivasan, "PyLLE: A fast and user friendly Lugiato-Lefever equation solver," *J. Res. Nat. Inst. Standards Technol.*, vol. 124, May 2019, Art. no. 124012.

[51] C. Godey, I. V. Balakireva, A. Coillet, and Y. K. Chembo, "Stability analysis of the spatiotemporal Lugiato-Lefever model for Kerr optical frequency combs in the anomalous and normal dispersion regimes," *Phys. Rev. A, Gen. Phys.*, vol. 89, no. 6, Jun. 2014, Art. no. 063814.

[52] N. Vermeulen, "Perspectives on nonlinear optics of graphene: Opportunities and challenges," *APL Photon.*, vol. 7, no. 2, Feb. 2022, Art. no. 020901.

[53] S. A. Mikhailov, "Theory of the strongly nonlinear electrodynamic response of graphene: A hot electron model," *Phys. Rev. B, Condens. Matter*, vol. 100, no. 11, Sep. 2019, Art. no. 085403.

[54] H. R. Philipp, "Optical properties of silicon nitride," *J. Electrochem. Soc.*, vol. 120, no. 2, p. 295, 1973.

[55] Y. Wang, C. Yang, and C. Bao, "Vernier frequency locking in counter-propagating Kerr solitons," *Phys. Rev. Appl.*, vol. 20, no. 1, Jul. 2023, Art. no. 014015.

[56] G. Nousios, T. Christopoulos, O. Tsilipakos, and E. E. Kriezis, "Integrated lasers with transition-metal-dichalcogenide heterostructures: Analysis and design utilizing coupled-mode theory for two-dimensional materials," *Phys. Rev. Appl.*, vol. 19, no. 6, Jun. 2023, Art. no. 064027.

[57] D. Chatzidimitriou, G. Nousios, T. Christopoulos, and E. E. Kriezis, "Theoretical study of a passively mode-locked integrated laser based on transition-metal dichalcogenides and graphene," *Phys. Rev. A, Gen. Phys.*, vol. 109, no. 4, Apr. 2024, Art. no. 043522.

[58] A. Krasnok, M. Tymchenko, and A. Alù, "Nonlinear metasurfaces: A paradigm shift in nonlinear optics," *Mater. Today*, vol. 21, no. 1, pp. 8–21, Jan. 2018.

Alexandros Pitilakis (Senior Member, IEEE) received the Diploma degree in electrical engineering from the School of Electrical and Computer Engineering, Aristotle University of Thessaloniki (AUTH), Greece, in 2005, the M.Sc. degree in electrical engineering from the ENST (Telecom), Paris, in 2007, including an internship at the Alcatel-Lucent Optical Transmission Systems Group, Marcoussis, France, and the Ph.D. degree in electrical engineering from the School of Electrical and Computer Engineering, AUTH, in 2013. He is currently a Post-Doctoral Researcher with AUTH, affiliated with the University of Western Macedonia (UoWM) and the National Hellenic Research Foundation (NHRF), and has taught undergraduate optics, photonics, and antennas and propagation courses at UoWM and AUTH, from 2016 to 2023. His research interests include theoretical and computational electromagnetics, waveguides and antennas (optical, THz, RF), metamaterials, nonlinear optics, integrated photonics, plasmonics, and graphene. He is a member of Optica.

Emmanouil E. Kriezis (Senior Member, IEEE) received the Diploma and Ph.D. degrees in electrical engineering from the School of Electrical and Computer Engineering, Aristotle University of Thessaloniki, Thessaloniki, Greece, in 1991 and 1996, respectively. In 1998, he joined the Department of Engineering Science, University of Oxford, Oxford, U.K., initially as an Engineering and Physical Sciences Research Council Post-Doctoral Researcher. Since 2004, he has been a Professor of optical and microwave communications with the School of Electrical and Computer Engineering, Aristotle University of Thessaloniki. His current research interests include nonlinear effects at optical frequencies, plasmonics, silicon photonics, graphene devices, and liquid crystal photonics. In 2001, he received the prestigious Royal Society University Research Fellowship to study light propagation in complex anisotropic media.